FULL PAPER

Enhanced Antitumor Efficacy by 808 nm Laser-Induced Synergistic Photothermal and Photodynamic Therapy Based on a Indocyanine-Green-Attached $W_{18}O_{49}$ Nanostructure

Kerong Deng, Zhiyao Hou, Xiaoran Deng, Piaoping Yang, Chunxia Li, and Jun Lin**

A novel nanoplatform based on tungsten oxide ($W_{18}O_{49}$, WO) and indocyanine green (ICG) for dual-modal photothermal therapy (PTT) and photodynamic therapy (PDT) has been successfully constructed. In this design, the hierarchical unique nanorod-bundled $W_{18}O_{49}$ nanostructures play roles in being not only as an efficient photothermal agent for PTT but also as a potential nanovehicle for ICG molecules via electrostatic adsorption after modified with trimethylammonium groups on their surface. It is found that the ability of ICG to produce cytotoxic reactive oxygen species for PDT is well maintained after being attached on the WO, thus the as-obtained WO@ICG can achieve a synergistic effect of combined PTT and PDT under single 808 nm near-infrared (NIR) laser excitation. Notably, compared with PTT or PDT alone, the enhanced HeLa cells lethality of the 808 nm laser triggered dual-modal therapy is observed. The in vivo animal experiments have shown that WO@ICG has effective solid tumor ablation effect with 808 nm NIR light irradiation, revealing the potential of these nanocomposites as a NIR-mediated dual-modal therapeutic platform for cancer treatment.

1. Introduction

Various near-infrared (NIR)-based therapeutic and interventional strategies, for example, photothermal therapy, photodynamic therapy, are currently under research in intensive preclinical and clinical investigations for cancer.[1] Here, NIR region (700–1100 nm) is a so-called transparency window for biological window, leading to the deep penetration and low absorption of light.[2] Because of unsatisfactory effects of single therapeutic treatment, many efforts for development of NIR-based synergistic effect of photothermal therapy (PTT) and photodynamic therapy (PDT), have been made to optimize the unsatisfactory results of tumor ablation.[3] Meanwhile, compared with PTT or PDT alone, combination therapy can not only avoid administration of multiple doses of agents to minimize the side effects, but it can also dramatically improve therapeutic efficacy.[4] A current alternative combined strategy is to design one unit with simultaneous PTT and PDT triggered by a single NIR laser. However, it is still a great challenge due to the particular requirement of the overlap both optical absorption of photothermal agents (PAs) and photosensitizers (PSs) in the NIR region so far.

In the PTT protocol, certain nanomaterials with localized hyperthermal effects under NIR light irradiation, such as graphene oxide,[5] gold nanostructures,[6] copper sulfide,[7] have still garnered immense research for cancer therapy. Alternatively, tungsten oxide nanocrystals, a kind of transition metal oxides, are currently explored to be an excellent potential PA for PTT.[8] Due to its strong localized surface plasmon resonances, nanostructured tungsten oxide can absorb NIR light with high efficiency to generate heat.[9] In recent studies, $W_{18}O_{49}$ nanomaterials have been reported to act as 980 nm laser-driven PAs or even $W_{18}O_{49}$ nanowires-mediated photodynamic therapy under 980 nm light irradiation.[10] However, 980 nm is at the rising edge of the absorption of tissue (although much lower than visible light) and can be absorbed by water.[11] The absorbed light energy would transform into thermal energy to cause an unnecessary heating effect on normal tissues, which would limit the power of the excitation light and pose a threat to their in vivo application.[12] Compared with 980 nm light, 808 nm NIR light as the excitation source to trigger PAs may overcome the overheating effect, since the water absorption is less than 1/20 of that at 980 nm.[13]

PDT is carried out via PSs and ultimately yields cytotoxic reactive oxygen species (ROS) to render apoptotic and necrotic

Dr. K. Deng, Dr. Z. Hou, Dr. X. Deng, Dr. C. Li, Prof. J. Lin
State Key Laboratory of Rare Earth Resource Utilization
Changchun Institute of Applied Chemistry
Chinese Academy of Sciences
Changchun 130022, P. R. China
E-mail: zyhou@ciac.ac.cn; jlin@ciac.ac.cn
Dr. K. Deng, Dr. X. Deng
University of Chinese Academy of Sciences
Beijing 100049, P. R. China
Prof. P. Yang
Key Laboratory of Superlight Materials and Surface Technology
Ministry of Education
College of Material Sciences and Chemical Engineering
Harbin Engineering University
Harbin 150001, P. R. China

DOI: 10.1002/adfm.201503046

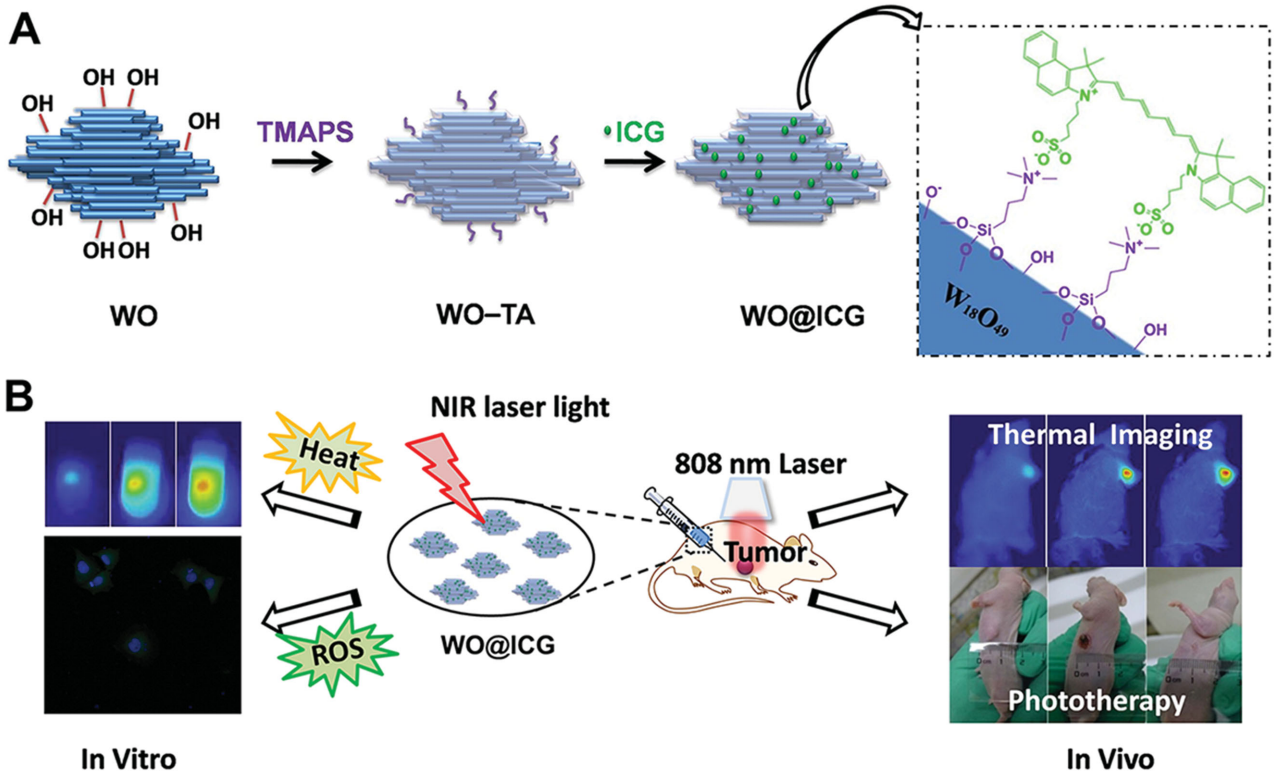

Scheme 1. A) Schematic illustration of the synthetic procedure of WO@ICG nanocomposites, including the manner of an ICG molecule absorbed to WO-TA samples via electrostatic interaction. B) In vitro and in vivo photothermal and photodynamic properties under 808 nm laser irradiation, including therapeutic potential in cultured HeLa cells and HeLa tumors xenograft model.

cell death. In medical procedure of PDT, photosensitized ROS production is widely exploited to remove the undesired tissue (e.g. cancers).[14] Up to now, most PSs respond mainly to visible or even ultraviolet light. The limited penetration depth and potential photodamage might hamper these PSs for in vivo bioapplications.[15] In particular, indocyanine green (ICG), an amphiphilic cyanine compound, can be triggered impressively by NIR light to producing ROS. Such novel optical property allows deeper tissue penetration and makes ICG molecules act as a potential NIR-induced mediator for clinical bioapplications.[16] Although recent reports have uncovered a few nanocomposites for combined PTT and ICG-mediated PDT, which exhibited in vitro and in vivo synergistic therapeutic activities under 808 nm NIR light,[17] simple and new types of nanovehicles merged with ICG molecules for NIR-triggered phototherapy are still needed.

In this study, an ICG attached $W_{18}O_{49}$ nanoplatform has been constructed aiming to achieve a synergistic effect of combined PTT and PDT on solid tumor under single 808 nm NIR light irradiation. In this design, $W_{18}O_{49}$ (WO) nanostructures act as not only an efficient photothermal agent, but also a potential nanocarrier for photosensitizers loading through physical interaction or chemical conjugation due to its hierarchical unique nanorod-bundled nanostructures (NRBs). Briefly, the surface hydroxyl groups of tungsten oxide (W–OH) which is of negative charges and weak binding affinity, were conjugated with *N*-trimethoxysilylpropyl-*N*,*N*,*N*-trimethylammonium chloride (TMAPS) for cationic functional groups. The TA groups-modified WO nanostructures were successfully obtained via condensation process of W–OH with methoxy groups from TMAPS, and then trapped ICG molecules via electrostatic adsorption (**Scheme 1**), which renders an efficient 808 nm light-based combined phototherapeutic agent. Such NIR light-based nanomaterials could produce local hyperthermia and ROS efficiently when exposed to 808 nm light, thus the in vivo synergistic effects of WO@ICG would be revealed. Moreover, compare with PTT or PDT alone, the as-prepared WO@ICG achieved superior antitumor effect with a low dose, which could also avoid the side effects of high injected dose of therapeutic agents.

2. Results and Discussion

2.1. Physical and Chemical Characterization of the WO@ICG

The WO NRBs were prepared by a modified solvothermal method using WCl_6 as the tungsten source.[18] The physicochemical characteristics of as-obtained products were examined by transmission electron microscope (TEM), scanning electronic microscopy (SEM), and X-ray diffraction (XRD). **Figure 1**A presents a unique TEM image (inset for SEM image) of WO NRBs obtained after 12 h of reaction. The resulting nanomaterials possess uniformly nanostructures (≈230 nm in width) in the form of nanorods bundled which are not densely packed together especially at the ends of the bundles. The

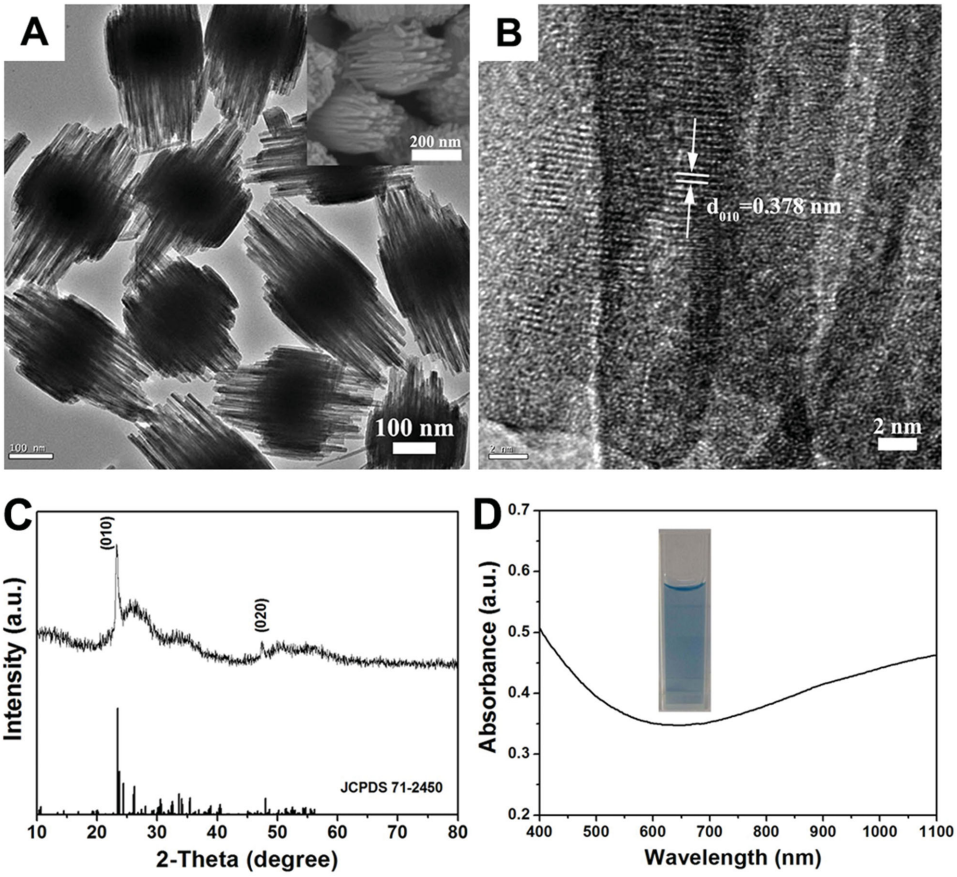

Figure 1. Characterization of $W_{18}O_{49}$ NRBs: A) TEM image (inset: SEM image), B) high-resolution TEM images, respectively. C) X-ray powder diffraction pattern of as-obtained WO and standard data for $W_{18}O_{49}$ (JCPDS 71–2450). D) UV–vis–NIR absorption spectrum of WO suspensions.

high-resolution TEM image in Figure 1B indicates the interplanar distances between adjacent lattice planes (0.378 nm) is well coincident with the (010) lattice of $W_{18}O_{49}$. The pure phase of WO samples is identified by XRD spectrum (Figure 1C). The optical property of as-obtained WO NRBs was also studied using UV–vis–NIR spectroscopy. As depicted in Figure 1D, the aqueous solution of WO NRBs presents blue color and its UV–vis–NIR spectrum displays an extended absorption band in the NIR region due to their intense localized surface plasmon resonances. This important feature of WO suggests us to test their ability for photothermal therapy. Figure S1 of the Supporting Information displays the temperature change of deionized water containing WO nanoparticles with various concentrations. Negligible temperature increase was observed in pure water group under NIR light irradiation for 5 min. However, under the same condition, WO groups could produce remarkable bulk heating. This result demonstrated the great NIR light irradiated heat generation capacity of WO nanoparticles for PTT.

Moreover, the near-infrared fluorescent dye ICG was chosen as a medium endowed WO with potential ability for PDT due to its matched NIR absorption. In addition, owning to one cationic pyrrolium group and two anionic sulfonic groups per one ICG molecule, the total charge shows minus one at neutral pH. It allows the ICG molecule to be attached on nanomaterials via strong electrostatic attraction in the neutral condition. TMAPS were introduced to help the formation of WO NRBs with TA terminal groups (designated as WO-TA) with relatively positive charges. The Fourier transform infrared (FT-IR) spectra (Figure S2, Supporting Information) show the characteristic absorption bands of ν (C–H) of TA groups at 2930 and 2858 cm^{-1} appear, indicating the TMAPS were successfully bonded to the surface of WO NRBs.[19] The process of ICG molecules loaded on WO-TA NRBs, designated as WO@ICG, was performed in methanol solution. Based on the UV–vis absorption results, the maximum amount of ICG attached was determined as 6.25 μg of ICG per mg of the WO@ICG complex. And for effectively producing enough ROS for PDT under 808 nm light exposure, we chose this proportion between WO and ICG of WO@ICG in our following experiments. Furthermore, the surface properties of pure WO, WO-TA, and WO@ICG samples were characterized by ζ-potential measurements in deionized water. As depicted in Figure S3 of the Supporting Information, pure WO with the abundant hydroxyl groups (W–OH) showed the lowest ζ-potential (–44.8 mV). In contrast, WO-TA exhibited relatively positive charged surfaces (–14.9 mV), indicating the successful TA groups coating. After conjugated with ICG, the slight decrease in the ζ-potential of WO@ICG (–23.8 mV) was observed, as previous studies reported.[20] In addition, the sizes of the WO@ICG nanocomposites in water and PBS buffer were measured by dynamic light scattering. As

shown in Figure S4 of the Supporting Information, the sizes of those nanoparticles showed negligible change in water and PBS even after a week, indicating the good stability of the composite nanoparticles. We have also tested the stability of WO@ICG in the neutral condition, the ICG content in supernatant of WO@ICG solution after 2 d mild shaking have been measured by UV–vis spectroscopy. No noticeable ICG absorption was detected, which shows the WO@ICG complex could be further applied to in vitro and in vivo cancer treatments.

2.2. Extracellular and Intracellular ROS Production

The effective PDT requires effective production of ROS surround the tumor sites. In order to verify the capability to produce cytotoxic ROS of WO@ICG under 808 nm laser irradiation, a chemical method by using 1,3-diphenylisobenzofuran (DPBF) probe as an acceptor of ROS was carried out.[21] **Figure 2**A represents the absorption of DPBF solution with WO@ICG samples at various irradiation times, indicating WO@ICG NRBs could effectively produce ROS under 808 nm light exposure. Furthermore, the absorption behaviors of NIR light alone and WO with DPBF solution exposed to NIR light were also investigated and compared. As shown in Figure 2B, there is no noticeable change of BPDF absorption in NIR light alone group or WO group under the laser irradiation. As we expected, the presence of ICG on WO@ICG samples could result in the high rate of decay of DPBF due to the continuous generation of ROS, confirming their ability to produce ROS.

We have also assessed the formation of ROS in HeLa cells induced by WO@ICG after NIR light irradiation, using nonfluorescent dichlorofluorescein diacetate (DCFH-DA) as a fluorogenic marker for ROS.[22] In the presence of ROS, DCFH-DA becomes oxidized to fluorescent dichlorofluorescein (DCF), which can emit bright green fluorescence. The DCF fluorescence in live cells was evaluated by fluorescence microscopy. According to the results shown in Figure 2C, no obvious green fluorescence is observed in control cells without 808 laser irradiation. While under NIR light irradiation, HeLa cells internalized with WO@ICG exhibit high amount of ROS. This result suggests that WO@ICG nanomaterials can induce ROS generation in live cells with the presence of NIR light, thus being a potential photodynamic agent for PDT. In addition, the NIR-mediated WO@ICG induced mitochondrial damage in HeLa cells was also investigated by JC-1 staining. It has been proved that mitochondrial polarization is indicated by a change in the ratio of red/green fluorescence intensity. As shown in **Figure 3**, it is clearly evident that there is no obvious green fluorescence in HeLa cells internalized with WO@ICG in the dark. However, upon exposure to 808 nm laser light, the JC-1 red fluorescence significantly decreased and strong green fluorescence was observed. Thus the above results clearly demonstrate the NIR light-drived combined effects of WO@ICG could produce ROS

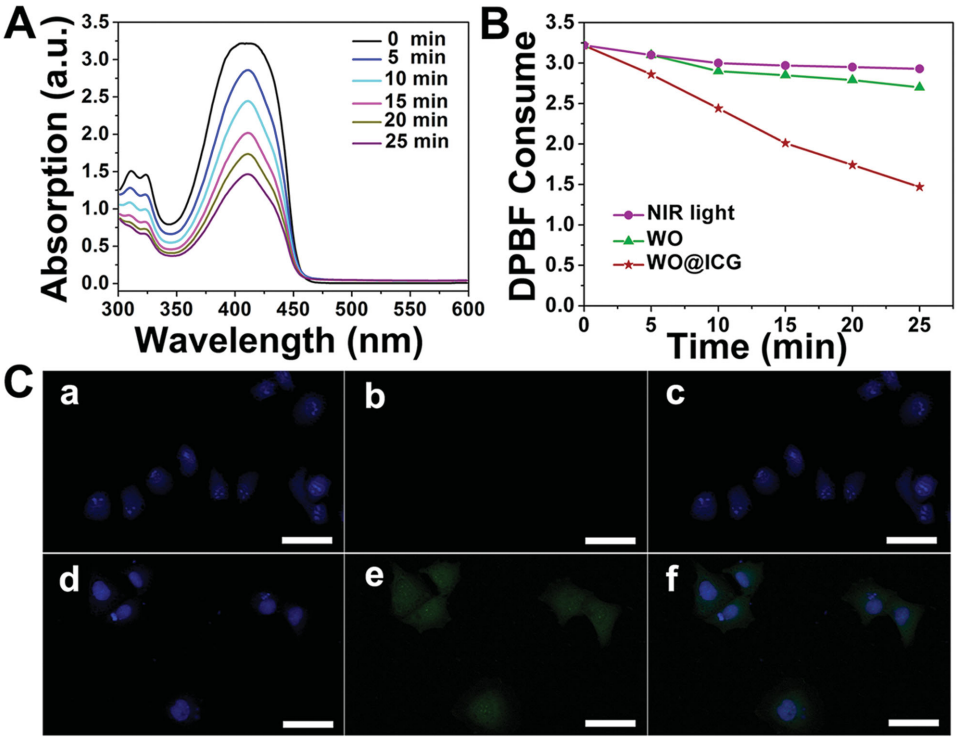

Figure 2. The generation of reactive oxygen species: A) Absorption spectra of DPBF solution incubated with WO@ICG under irradiation at 808 nm for different time; B) Absorption at 410 nm of DPBF as a functional of 808 nm light radiation time (DPBF alone, incubated with WO, and incubated with WO@ICG, respectively); C) Intracellular ROS generation was detected in HeLa cells treated with WO@ICG a–c) before and d–f) after 808 nm laser irradiation. Each series can be classified to blue fluorescence from nuclei of the cells stained by Hoechst 33324 (left column), green fluorescence from DCF indicating the presence of singlet oxygen (middle column) and overlay of both above (right column), respectively. All scale bars are 50 μm.

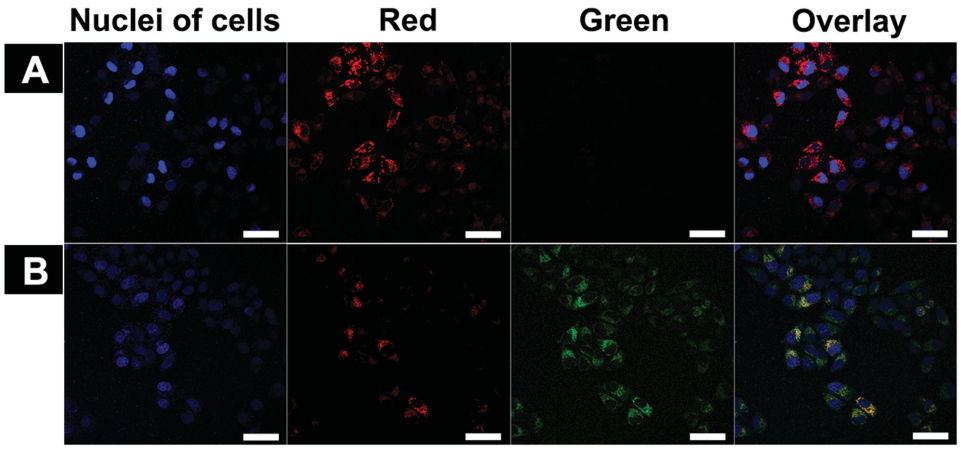

Figure 3. NIR-mediated PDT induced mitochondrial damage in HeLa cells A) with WO@ICG under NIR light irradiation and B) control group. Increase of green fluorescence in irradiated cells suggests loss of mitochondrial membrane potential. Each series can be classified to nuclei of cells being dyed blue by Hoechst 33324, JC-1 forming red-emitting aggregates in the mitochondrial matrix, green-emitting monomers in the cytoplasm, overlapped image of the three above. All scale bars are 50 μm.

efficiently and result in hyper-polarize of the mitochondria membrane potentials.

2.3. In Vitro Cytotoxicity and Phototoxicity of WO@ICG

To investigate the in vitro cytotoxicity and phototoxicity to cancer cells of WO and WO@ICG, the standard methyl thiazolyl tetrazolium (MTT) assay was carried out to determine the relative viabilities of HeLa cells. After cells were cultured with various concentrations of WO and WO@ICG in the dark for 24 h, no any noticeable cellular death is observed when treated with either WO or WO@ICG even at a high concentration of 800 μg mL^{-1} in the dark (Figure S5, Supporting Information). However, as described in **Figure 4**A, it leads to a drastic drop in the percentage of cell viabilities in the both two groups upon exposure to 808 nm light (1.5 W cm^{-2} for 5 min). This result indicates these samples are active in photoinduced cancer cell killing. Interestingly, the WO@ICG exhibits enhanced HeLa cell lethality in a dose-dependent manner compared with WO group under the identical condition. For instance, the death of cell incubated with WO@ICG (100 μg mL^{-1}) is almost as high as that of WO (500 μg mL^{-1}). To better elucidate the toxic effect of every individual element (808 nm laser light, WO or

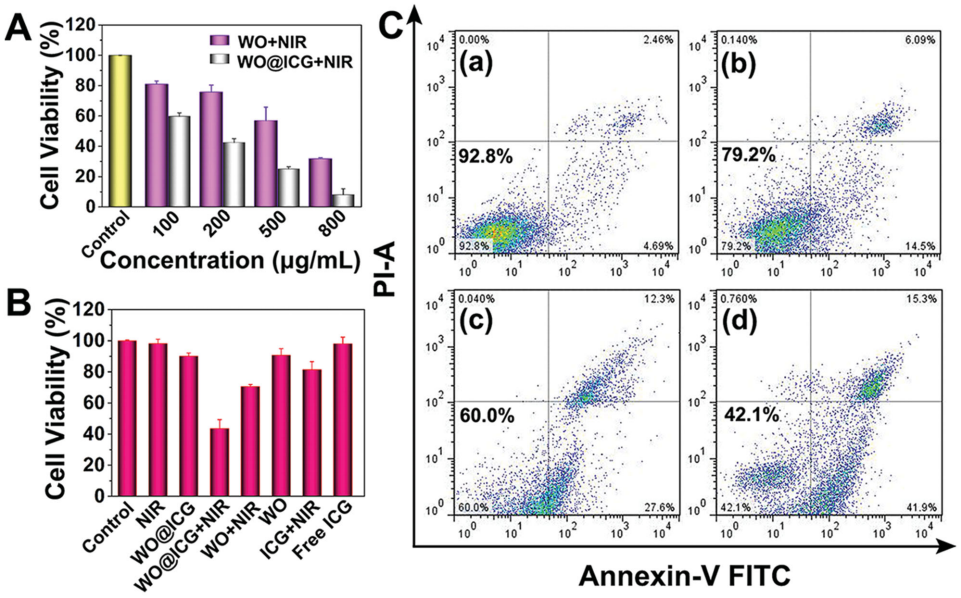

Figure 4. In vitro evaluation of HeLa cell viabilities after phototherapy treatment with A) different concentrations of WO and WO@ICG exposed to 808 nm laser light and B) various formulas, estimated by MTT proliferation test, respectively. Error bars indicate standard deviations, $n = 3$. C) Flow cytometric analyses of apoptosis of HeLa cells by staining with Annexin V-FITC and PI after NIR light mediated PTT/PDT treatment with various formulas (a) control; b) ICG + NIR light; c) WO + NIR light; d) WO@ICG + NIR light).

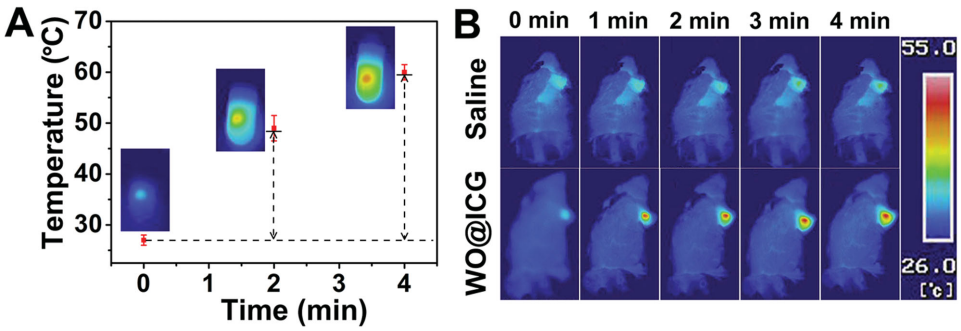

Figure 5. A) Representative photographs of temperature change behavior of WO@ICG in water under different irradiation times. Error bars indicate standard deviations, $n = 3$. B) IR thermal images of tumor-bearing mice with or without WO@ICG injection exposed to the NIR laser at power densities of 1.5 W cm^{-2} recorded at different time intervals, respectively.

ICG) on HeLa cell viabilities, a systematical study was carried out afterward. As shown in Figure 4B, neither NIR irradiation only group nor the specific concentration of single element groups (WO, WO@ICG, and free ICG with the equivalent ICG concentration of WO@ICG) could give rise to higher amount of cell death. By contrast, similar NIR illumination of WO@ICG did lead to greater cytotoxicity. Therefore, it could be demonstrated that ICG-mediated PDT effect from WO@ICG makes great contribution to the improved phototoxicity. Additionally, the flow cytometry data in Figure 4C, intuitively evidence the synergistic effects of combined PDT and PTT of WO@ICG in agreement with the above MTT results. Compared with PTT from WO or PDT from ICG, a large amount of apoptosis and necrosis of HeLa cells were caused by NIR-triggered combined PTT and PDT treatment. Additionally, the dose-dependent apoptotic effect of NIR-drived WO@ICG in HeLa cells is also observed from Figure S6 of the Supporting Information. Due to the laser caused hyperthermia for cancer treatment is nonspecific, it is necessary to choose the appropriate laser parameters to obtain effective phototherapeutic response and in the meanwhile ensure the laser illumination safety to surrounding normal tissues.[23] As we see, the cell viability is nearly 87.8% after 10 min NIR light irradiation, demonstrating that 10 min laser irradiation (1.5 W cm^{-2}) does not damage the cells when there are no nanomaterials incubation.

Overall, the in vitro results clearly point toward the conclusion that 808 nm light-drived combined effects of WO@ICG can generate high amount of ROS and induce high amounts of apoptotic and necrotic cells.

2.4. In Vitro and In Vivo Photothermal Property of WO@ICG

Inspired by these data, which revealed the rather effective cancer cells damage of our theranostic nanomaterials, we would like to use WO@ICG for in vivo cancer treatment. To understand how the temperature changes during the 808 nm light irradiation based combined therapy process, we carried out an intratumoral injection experiment to investigate the photothermal effects of WO@ICG using mice with tumors. First, it is noted that ICG can also be used as a photothermal agent, thus the photothermal properties of WO and WO@ICG (both 0.8 mg mL^{-1}) under 808 nm laser irradiation have been investigated to understand the effect of ICG loading on the synergistic photothermal effect of WO@ICG nanomaterials. As shown in **Figure 5**A and Figure S7 of the Supporting Information, there is no obvious difference in temperature rising between the two groups under irradiation of 808 nm laser light. It might be inferred that such amount of ICG loading cannot affect the photothermal effect. Additionally, previous work had pointed out that although the photothermal conversion ability of ICG is strong, it would quickly diminish after multiple rounds of laser irradiation.[24] Compared with small molecules ICG for PPT, WO nanoparticles exhibit strong photothermal stability under 808 laser irradiation.[9] Consisting with the in vitro the thermal effect of WO@ICG, the local temperature of tumor with WO@ICG injected increased rapidly up to 49 °C within 4 min, whereas no noticeable temperature rise in the control group injected with saline (Figure 5B). In the PTT field, controlled localized temperature increments (within the 41–48 °C temperature range) have shown signs of apoptosis on tumor cells, which is sufficient to kill tumor cells.[25] As explained by the results, the WO@ICG indeed cause photo-heat conversion efficiently in vivo and it can be used as hyperthermia agents for cancer therapy.

2.5. In Vivo Destruction of Tumor in Mice

As a proof-of-concept study, the in vivo therapeutic efficiencies of PTT and PDT combined therapy were assessed using HeLa tumors xenograft model in nude mice. Here, as controls, group 1 received saline injected only, group 2 received nothing intratumoral injection but exposed to 808 nm laser light. Compared with group 1, group 2 shows no such significant antitumor effect (**Figure 6**A), suggesting that NIR laser at such a power density itself could not induce obvious damage. In contrast, the mice treated with 808 nm laser irradiated WO@ICG shows much lower tumor growth. Remarkably, by 21 d after combined treatment, the skin of mice at the irradiation site in treated group peeled off and new skin was developed. This result indicated the good tumor growth inhibition by WO@ICG. The digital photos of excised tumors from representative mice (Figure 6B) visually display that the tumor size for combined therapy treated with WO@ICG under 808 nm light is the smallest, confirming an extra tumor

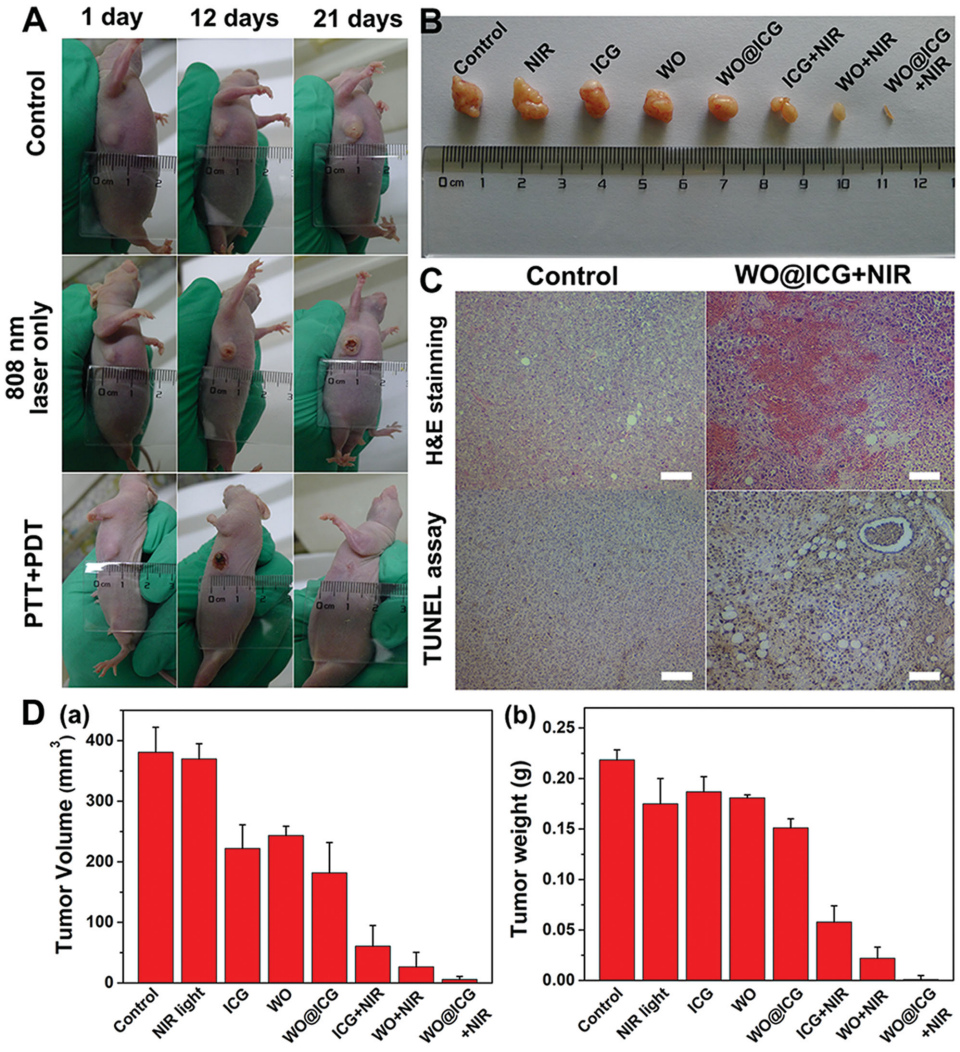

Figure 6. A) Representative photographs of mice after different treatments: without anything, 808 nm laser irradiation only and WO@ICG exposed to 808 nm light, respectively. B) Photographs of tumor tissue obtained in different groups after 21 d treatment, respectively. C) Representative images of H&E stained tumor sections and the tumor sections examined by TUNEL assay from the control group and WO@ICG treated phototherapy group, respectively. The scale bars are 50 μm. D) The a) tumor volume and b) tumor weight of mice bearing HeLa tumor in different groups after treatment. Error bars indicate standard deviations, $n = 5$.

inhibition effect of the WO@ICG. Compared with the mice groups injected pure ICG, WO or WO@ICG without NIR light, the laser-irradiated mice groups achieved PTT or PDT alone shows an obvious reduction in tumor growth. Moreover, the change in tumor volumes and weight of only NIR irradiation group (Figure 6D) revealed little inhibitory effects on the solid tumors growth, which demonstrates the negligible thermal damage of NIR light. Interestingly, the treatment of WO@ICG with 808 nm light leads a significantly slower tumor growth rate attributable to the enhanced combination therapy of PTT and PDT. Such in vivo results are consistent with that obtained from the cellular experiments. In brief, this fact illustrates the combination of overheating effect obtained from WO exerted PTT modality and ROS derived from ICG-mediated PDT have achieved enhanced therapeutic efficacy over than that of PDT or PTT alone and obtained a desirable phototherapy outcome in vivo.

2.6. Histology and Hematology Results of the Mice Injected with WO@ICG

After combined phototherapy, the tumors were also histologically examined at the cellular level (Figure 6C and Figure S8, Supporting Information). By stained with hematoxylin and eosin (H&E), necrosis of the tumor tissue is clearly observed. Compared with the control group, total destroyed cells after WO@ICG treated phototherapy were found. In situ TUNEL staining was also introduced on tissue sections of tumors to study the ability of NIR light mediated phototherapy to elicit apoptosis of tumor cells. Consistent with the above observation, the high degrees of tumor cell necrosis and apoptosis (dark brown nuclei) in the combination therapy group are observed in that region, which has evidenced the tumor cell death after WO@ICG mediated phototherapy treatments under NIR light. With the purpose of assessing the in vivo biosafety of the

WO@ICG, the histological examination of the major organs excised from WO@ICG-injected nude mice at 15 d post-injection was tested. Notably, no appreciable adverse effect (e.g., necrosis or inflammatory response) to the examined major organs of treated mice is observed in Figure S9 of the Supporting Information, which confirms the favorable biocompatibility of WO@ICG in vivo.

2.7. The Long-Term Toxicity of WO@ICG Nanoparticles

The long-term toxicity of WO@ICG nanoparticles was also assessed by biodistribution, biochemical analyses, and weight fluctuation of healthy mice. The in vivo biodistribution was conducted by injecting WO@ICG nanomaterials at 20 mg kg^{-1} into the tail vein of healthy female Kunming mice. All of the major organs were surgically removed from the mice at timed intervals, and the W contents were measured by ICP-MS. As depicted in Figure S10 of the Supporting Information, the remaining WO@ICG was taken up predominantly by the spleen, liver and lung within the first 12 h. Then the level of W in the organs slightly decreased over time. And most of the nanoparticles were excreted from these organs after 14 d post-injection. The potential toxicology was studied via performing in vivo serum biochemistry of healthy mice on day 1, day 7, and day 14 post-intravenous administration of WO@ICG nanomaterials. The liver function makers (alanine aminotransferase–ALT and aspartate aminotransferase–AST), kidney function indicators (blood urea nitrogen–BUN), and heart function signals (creatine kinase–CK) in the test group were all measured. Encouragingly, these parameters appeared to be rather close to those of control group and fell within the normal reference ranges (**Figure 7**A–C), suggesting no obvious hepatic, kidney or heart disorder of mice intravenously injected with WO@ICG nanocomposites. The result helps us to relieve the concerns on the toxicity of these nanoparticles in vivo. Furthermore, the body weights of healthy mice intravenously injected with WO@ICG nanocomposites have also been recorded. As shown in Figure 7D, the body weights of the mice treated with different doses of WO@ICG nanocomposites (even up to 0.7 mg WO@ICG per mice), were all similar to that of control group, indicating the as-prepared WO@ICG nanoparticles have no evident toxic effects on healthy mice.

Hence, the above data collectively evidenced that combinatorial PTT and PDT of the WO@ICG nanomaterials can indeed improve the overall therapeutic effect successfully. Several studies have highlighted the combined PTT and PDT on one nanoplatform, but the PTT and PDT were implemented under respective laser irradiation.[26] Our strategy of exploiting ICG attached on WO-TA allows the synergistic effects under a single 808 nm laser for deeper tissue penetration, and enables the treatment of tumors located far from the body surface. More importantly, these results indicate that WO@ICG

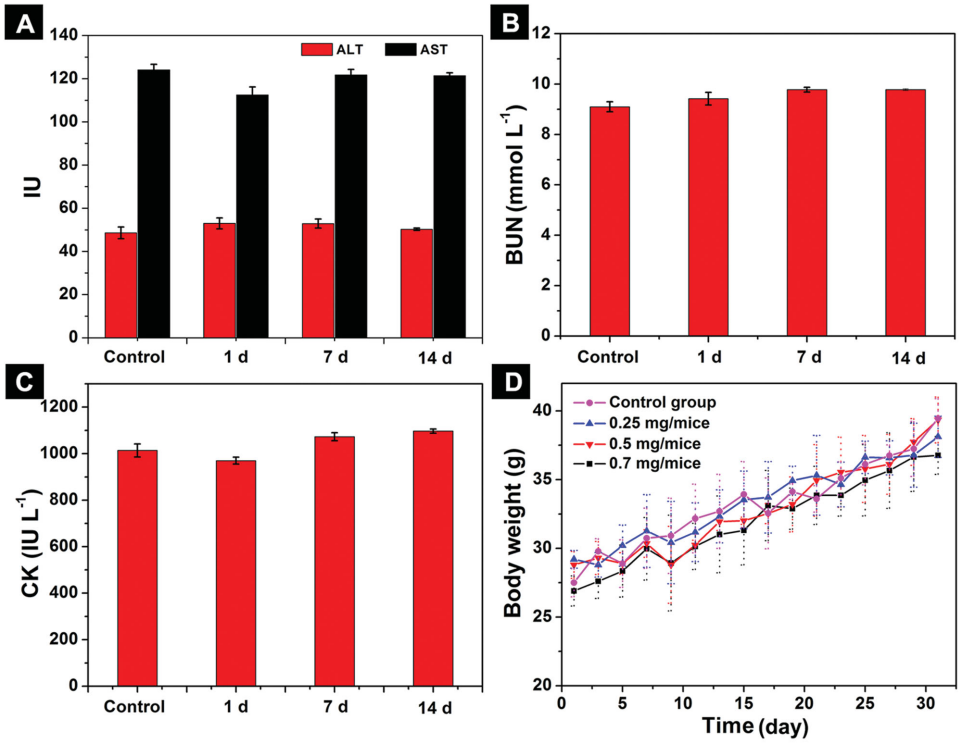

Figure 7. Serum biochemistry data including A) liver function markers (alanine aminotransferase (ALT), and aspartate aminotransferase (AST)), B) kidney function indicators (blood urea nitrogen (BUN) levels), and C) heart function signals (creatine kinase (CK)). Healthy female Kunming mice intravenously injected with WO@ICG nanocomposites were sacrificed at 1, 7 and 14 days post-injection for blood collection. Untreated healthy mice were used as the control. D) The body weight growth curves of the healthy mice injected with different doses of WO@ICG nanocomposites (0.25, 0.5, and 0.7 mg per mice) and without injection as control group. Error bars indicate standard deviations, $n = 5$.

nanocomposites could be a safe and more effective phototherapeutic candidate to cancer treatment.

3. Conclusion

In conclusion, a novel WO@ICG nanoplatform based on unique nanorods-bundled $W_{18}O_{49}$ nanostructures have been constructed for in vivo tumor photothermal and photodynamic dual-modality therapy using single 808 nm laser irradiation. This nanosystem exhibits little appreciable dark toxicity, while upon NIR light irradiation, it can concomitantly generate ROS from ICG and local hyperthermal from WO in vitro, thus leading to disruption of the mitochondria membrane and triggering remarkable tumor cell apoptosis/necrosis. We also elucidated the superior in vivo solid tumor inhibitory efficiency of the WO@ICG nanosystem over than PTT and PDT alone. In addition, histological examination showed no apparent toxicity of WO@ICG to the treated mice. All the data have demonstrated that the WO@ICG NRBs-mediated therapeutic nanoplatform achieves a remarkable synergist effect on in vivo solid tumor ablation with injection at low dose. More importantly, no evident toxic effects induced by WO@ICG were observed in our experiments. We believe that the design of WO@ICG NRBs holds great promise in solid tumor treatments.

4. Experimental Section

Materials and Reagents: WCl_6 (99.9%) and indocyanine green (ICG) were purchased from Aladdin industrial Inc. n-Trimethoxysilylpropyl-n,n,n-trimethylammonium chloride (TMAPS, 50% in methanol) was obtained from J&K Scientific. N-propanol, methanol, and toluene were obtained from Beijing Chemical Works. All the organic solvents were analytical grade and used as received.

Synthesis of $W_{18}O_{49}$ Nanomaterials: $W_{18}O_{49}$ nanomaterials were prepared according to the previous literature.[27] Typically, WCl_6 (0.1785 g) was dissolved in n-propyl alcohol (30 mL), and the solution was then forming a transparent yellow solution under magnetically stirring. After 15 min, the above mixing solution was transferred into a Teflon-lined stainless steel autoclave and sealed, maintained at 200 °C for 12 h. The blue precipitate was collected by centrifugation and washed several times with deionized water and ethanol. Finally, the final precipitate was directly dispersed into methanol.

Preparation of WO-TA Samples: The TMAPS-modified WO NCs were synthesized through a modified method.[28] Briefly, the as-obtained WO samples were dispersed in 20 mL mixture solution of methanol/toluene (volume ratio = 1:1). The mixture was heated to 95 °C till a half of the solvent was evaporated. Thereafter, methanol was added. The process was repeated three times to ensure the solution was completely anhydrous. Finally, the solvent was fixed to 20 mL by addition of methanol followed by adding 400 µL TMAPS and stirred for 10 h at 70 °C under N_2. The product was washed with anhydrous ethanol and distilled water several times.

Preparation of WO@ICG Samples: First, the dye ICG solution was prepared by mixing ICG (1 mg) in methanol (1 mL). Then the stock solution of ICG was diluted in methanol to a concentration of ICG (25 µg mL^{-1}) in methanol. For ICG loading, the process was as follows: 15 mg as-obtained WO-TA samples were dispersed into 10 mL of the diluted ICG solution. The mixture was constantly stirred overnight in the dark. The WO@ICG complex was finally separated by centrifugation and washed several times with deionized water, and then dispersed in bacteria-free water for further applications. The amount of ICG loading on WO-TA samples was determined by measuring the decrease in optical absorption of the residual solution at 395 nm.

Photothermal Effect of WO in Aqueous Solution: The aqueous solution of WO with different concentrations was irradiated using an 808 nm laser (BWT Beijing Ltd., China) with a power density of 1.2 W cm^{-2} over a period of 5 min. The temperature of solution was captured by a digital thermometer with a thermocouple probe.

Cell Culture: The HeLa cells line was cultured in DMEM culture medium supplemented with 1% (v/v) penicillin, 1% (v/v) streptomycin, and 10% (v/v) fetal bovine serum at 37 °C in 5% CO_2.

Extracellular and Intracellular ROS Detection: The generation of extracellular ROS was measured with a DPBF probe. Briefly, 2 mL of ethanol solution containing DPBF (10 mM) was added to 2 mL of WO@ICG solution (15 mg), and then the solution was kept in the dark with magnetic stirring and irradiated by an 808 nm NIR laser for various time periods. Then, the solution was centrifuged at 10 000 rpm, and the supernatant was collected for UV–vis detection (410 nm). The effects of NIR light irradiation alone and WO samples (15 mg) were also detected by the same process.

A ROS-sensitive probe, DCFH-DA, which could be oxidized to the highly fluorescent DCF by ROS, was chosen to detect the intracellular generation of ROS. After a 6 h incubation of HeLa cells in the dark with WO@ICG, noninternalized NCs were washed with PBS, and fresh culture media containing DCFH-DA (20 µm) was added for another 1 h incubation in the dark. The HeLa cells were then irradiated with 808 nm light. After irradiation, the medium was replaced with PBS and fluorescence images of treated cells were acquired using a laser confocal microscope. For DCF detection, the excitation was 485 nm, and the emission wavelength was 525 nm.

In Vitro Assessment of Mitochondrial Membrane Potential Using JC-1: HeLa cells (1×10^6) in a 35 mm confocal dish were treated with WO@ICG, followed by additional 4 h incubation. After photo irradiation by 808 nm laser, the cells were washed with PBS, and added a serum-free medium containing JC-1 dye, subjected to additional 20 min incubation at 37 °C. Finally, the cells were subjected trypsinization and washed with cold JC-1 buffer solution two times before visualized of the green and red fluorescence levels using a laser confocal microscope. The images were obtained at 488 nm excitation and 530 nm emission for green (JC-1 monomers) and at 543 nm excitation and 590 nm emission for red fluorescence (JC-1 aggregates).

In Vitro Cytotoxicity Evaluation: The in vitro dark-cytotoxicity of WO and WO@ICG were investigated by standard MTT assays using HeLa cell lines as model. Briefly, 5000 cells per well were seeded in a 96-well plate and incubated overnight. Then the cells were treated with different concentrations of WO and WO@ICG ranging from 12.5 to 800 µg mL^{-1}, respectively. After 24 h incubation, the medium containing NPs was removed and 20 µL of MTT solution was added into each well and cultured for another 4 h. Finally, the supernatant was replaced with 150 µL of dimethyl sulfoxide (DMSO) each well. The plate was shaken for 10 min and examined using a microplate reader (Therom Multiskan MK3) at the wavelength of 490 nm. Results were expressed as the percentage of cell viability.

For the combined photothermal and photodynamic therapy at the cellular level, HeLa cells (5000 per well) were placed in each well of a 96-well plate and incubated overnight. Then the cells were treated with at different concentrations (100, 200, 500, 800 µg mL^{-1}) of WO@ICG, and the same concentration of WO was used as the control. After 6 h incubation, the cells were exposed to an 808 nm laser at the energy density of 1.5 W cm^{-2} for 5 min and incubated for another 24 h. The viabilities of HeLa cells were evaluated using the MTT assay method. For systematical study on the toxic effect of these nanomaterials, WO (200 µg mL^{-1}), WO@ICG (200 µg mL^{-1}, [ICG] = 1.25 µg mL^{-1}), and pure ICG ([ICG] = 1.25 µg mL^{-1}) with NIR light irradiation (1.5 W cm^{-2}, 5 min) were added to the HeLa cells in a 96-well plate. In parallel, cells incubated with the same concentration of these nanomaterials without NIR light irradiation were also used as comparison. The cytotoxicity was evaluated after 24 h using the MTT assay, as indicated above. Same concentration of samples was used for the following studies.

For flow cytometry, HeLa cells were seeded in six-well culture plates and divided into three groups treated with ICG, WO, and WO@ICG, respectively. After NIR light irradiation (1.5 W cm^{-2}; 5 min), all Hela cells were incubated for further 3 h at 37 °C in the dark. Cells incubated with PBS without NIR light irradiation served as comparison. A single cell suspension was prepared consecutively by trypsinization, washing with cold PBS. Then the cells were stained by using an annexin V-FITC and PI staining kit from manufacturer's instructions (BestBio, Shanghai). The induction of apoptosis in HeLa cells were examined by a FACS Calibur flow cytometer (BD Biosciences).

Animal Xenograft Model: Female Balb/c nude mice (six weeks old) were purchased from Center for Experimental Animals, Jilin University. All animal studies were conducted in accordance with the guidelines of the National Regulation of China for Care and Use of Laboratory Animals. The HeLa tumor models were successfully established by subcutaneous injection of 4×10^6 cells suspended in 100 µL PBS into the right and left axilla of each mouse. The mice were treated when the tumor volumes approached 60×70 mm^3.

In Vivo Phototoxicity Study: Experiments were started when the tumor volumes approached 60 mm^3. The HeLa tumor-bearing nude mice were randomly distributed into eight groups ($n = 5$, each group), and 100 µL of the corresponding WO, WO@ICG or ICG was intratumorally injected into the tumor-bearing mice: 1) control group (only received PBS); 2) NIR irradiation only; 3) pure ICG administrated only (0.031 mg mL^{-1}); 4) WO administrated only (5 mg mL^{-1}); 5) WO@ICG administrated only (5 mg mL^{-1}); 6) pure ICG administrated (0.031 mg mL^{-1}) + NIR irradiated; 7) WO administrated (5 mg mL^{-1}) + NIR irradiated; 8) WO@ICG administrated (5 mg mL^{-1}) + NIR irradiated, respectively. All the groups received only one sample injection. Groups 1 and 2–4 were not irradiated after intratumoral injection. For NIR irradiated groups, the tumors were exposed to 808 nm laser of power density at 2 W cm^{-2} for 15 min (5 min break after 5 min irradiation) at 6 h post-injection, respectively. The therapeutic results of each group were evaluated by measuring the tumor volumes after 21 d. Tumor volume (V) = length × width^2/2. Relative tumor volume was calculated as V/V_0 (V_0 was the corresponding tumor volume when the treatment was initiated).

In Vivo Thermal Imaging: Suspension of H22 tumor cells was subcutaneously inoculated into the left armpit of female Kunming mice. When the tumor size reached about 100 mm^3, mice bearing tumor were intratumorally injected with WO@ICG suspension (100 µL, 1 mg mL^{-1}). The thermal imaging of different times after injection was recorded by a R300SR-HD infrared camera (NEC) when the tumors were exposed to 808 nm laser light.

Histology Examination: After 21 d from the phototherapy, the major organs (liver, lung, kidney, heart, and spleen) and tumor tissues from control and treated mice were excised, fixed in 4% paraformaldehyde solution and then processed routinely into paraffin. The sliced tissues were stained with H&E and examined by an inverted florescence microscope system (Nikon-Ti-S).

In Situ TUNEL Assay for Apoptotic Cells: Apoptotic cell death in the tumor tissue sections was also detected using the In Situ Cell Death Detection Kit (Roche Applied Science, Mannheim, Germany) according to the manufacturer's protocol. The fluorescence images of tumor tissue sections were obtained through a CLSM.

In Vivo Biodistribution and Biocompatibility of WO@ICG Nanoparticles: The 40 healthy female Kunming mice weighing about 25 g were treated with WO@ICG nanoparticles (20 mg kg^{-1}) by tail vein injection. The mice ($n = 5$) were then euthanized at different time points (30 min, 1 h, 3 h, 12 h, 1 d, 3 d, 7 d, and 14 d). Other five healthy mice were used as the untreated control group. Major organs (heart, liver, spleen, lung, and kidney) were collected and weighed. Then all the tissues were treated with HNO_3 and H_2O_2 (v/v = 1:1) at 70 °C to obtain clear solutions. The tungsten concentrations in the solutions were determined by ICP-MS and the contents in each tissue were calculated. For blood biochemistry assay, blood of the experimental groups (at 1, 7, and 14 d post-injection of WO@ICG nanoparticles) and control group were collected at the same time.

In addition, the 15 healthy female Kunming mice were randomly divided into three groups and treated by tail vein injection of different doses of WO@ICG nanoparticles (0.25, 0.5, and 0.7 mg per mice). The other five mice with nothing injection were used as control group. The body weights of the mice were monitored every 2 d for 30 d.

Characterization: The TEM and high-resolution transmission electron microscopy (HRTEM) of samples were imaged using a FEI Tecnai G2 S-Twin with a field emission gun operating at 200 kV. The SEM image was obtained using a field emission scanning electron microscope (FE-SEM, XL30, Philips). FT-IR spectra were obtained by a Perkin–Elmer 580BIR spectrophotometer using KBr pellets. X-ray diffraction measurements were performed a D8 Advanced diffractometer (Bruker) using CuKa radiation ($\lambda = 0.154$ nm). The UV–vis absorption spectra were obtained from U-3100 spectrophotometer (Hitachi). The dynamic light scattering and surface zeta potential measurements were performed on a Malvern instrument Zatasizer Nano. The inductively coupled plasma-mass spectrometer (ICP-MS) was taken on an iCAP 6300 of Thermo scientific.

Supporting Information

Supporting Information is available from the Wiley Online Library or from the author.

Acknowledgements

This project was financially supported by the National Natural Science Foundation of China (NSFC 51472233, 51332008, 51372243, 51422209), and National Basic Research Program of China (2014CB643803).

Received: July 22, 2015
Revised: September 22, 2015
Published online: November 6, 2015

[1] a) A. Master, M. Livingston, A. Sen Gupta, *J. Controlled Release* **2013**, *168*, 88; b) K. F. Chu, D. E. Dupuy, *Nat. Rev. Cancer* **2014**, *14*, 199; c) P. Rai, S. Mallidi, X. Zheng, R. Rahmanzadeh, Y. Mir, S. Elrington, A. Khurshid, T. Hasan, *Adv. Drug Delivery Rev.* **2010**, *62*, 1094.

[2] L. C. Mimun, G. Ajithkumar, M. Pokhrel, B. G. Yust, Z. G. Elliott, F. Pedraza, A. Dhanale, L. Tang, A.-L. Lin, V. P. Dravid, D. K. Sardar, *J. Mater. Chem. B* **2013**, *1*, 5702.

[3] a) S. Wang, P. Huang, L. Nie, R. Xing, D. Liu, Z. Wang, J. Lin, S. Chen, G. Niu, G. Lu, *Adv. Mater.* **2013**, *25*, 3055; b) J. Peng, L. Zhao, X. Zhu, Y. Sun, W. Feng, Y. Gao, L. Wang, F. Li, *Biomaterials* **2013**, *34*, 7905; c) X. Song, C. Liang, H. Gong, Q. Chen, C. Wang, Z. Liu, *Small* **2015**, *11*, 3932.

[4] a) Y. Yong, L. Zhou, Z. Gu, L. Yan, G. Tian, X. Zheng, X. Liu, X. Zhang, J. Shi, W. Cong, W. Yin, Y. Zhao, *Nanoscale* **2014**, *6*, 10394; b) T. Liu, C. Wang, X. Gu, H. Gong, L. Cheng, X. Shi, L. Feng, B. Sun, Z. Liu, *Adv. Mater.* **2014**, *26*, 3433.

[5] a) H. Zhang, H. Wu, J. Wang, Y. Yang, D. Wu, Y. Zhang, Y. Zhang, Z. Zhou, S. Yang, *Biomaterials* **2015**, *42*, 66; b) Y.-K. Kim, H.-K. Na, S. Kim, H. Jang, S.-J. Chang, D.-H. Min, *Small* **2015**, *11*, 2527; c) S. M. Sharker, J. E. Lee, S. H. Kim, J. H. Jeong, I. In, H. Lee, S. Y. Park, *Biomaterials* **2015**, *61*, 229.

[6] a) T. B. Huff, L. Tong, Y. Zhao, M. N. Hansen, J.-X. Cheng, A. Wei, *Nanomedicine* **2007**, *2*, 125; b) H. Chen, L. Shao, T. Ming, Z. Sun, C. Zhao, B. Yang, J. Wang, *Small* **2010**, *6*, 2272; c) E. Boisselier, D. Astruc, *Chem. Soc. Rev.* **2009**, *38*, 1759; d) L. Cheng, C. Wang, L. Feng, K. Yang, Z. Liu, *Chem. Rev.* **2014**, *114*, 10869.

[7] a) F. Lu, J. Wang, L. Yang, J.-J. Zhu, *Chem. Commun.* **2015**, *51*, 9477; b) Q. Tian, M. Tang, Y. Sun, R. Zou, Z. Chen, M. Zhu, S. Yang, J. Wang, J. Wang, J. Hu, *Adv. Mater.* **2011**, *23*, 3542; c) L. Zhang, S. Gao, F. Zhang, K. Yang, Q. Ma, L. Zhu, *ACS Nano* **2014**, *8*, 12250.
[8] a) H. C. Lin, C. Y. Su, C. K. Lin, *J. Nanopart. Res.* **2011**, *13*, 4549; b) Z. Liu, J. Liu, R. Wang, Y. Du, J. Ren, X. Qu, *Biomaterials* **2015**, *56*, 206.
[9] K. Manthiram, A. P. Alivisatos, *J. Am. Chem. Soc.* **2012**, *134*, 3995.
[10] a) Z. Chen, Q. Wang, H. Wang, L. Zhang, G. Song, L. Song, J. Hu, H. Wang, J. Liu, M. Zhu, D. Zhao, *Adv. Mater.* **2013**, *25*, 2095; b) Z. Zhou, B. Kong, C. Yu, X. Shi, M. Wang, W. Liu, Y. Sun, Y. Zhang, H. Yang, S. Yang, *Sci. Rep.* **2014**, *4*, 3653; c) P. Kalluru, R. Vankayala, C. S. Chiang, K. C. Hwang, *Angew. Chem. Int. Ed.* **2013**, *52*, 12332.
[11] a) H. Kobayashi, M. Ogawa, R. Alford, P. L. Choyke, Y. Urano, *Chem. Rev.* **2010**, *110*, 2620; b) Q. Zhan, J. Qian, H. Liang, G. Somesfalean, D. Wang, S. He, Z. Zhang, S. Andersson-Engels, *ACS Nano* **2011**, *5*, 3744.
[12] a) Y. F. Wang, G. Y. Liu, L. D. Sun, J. W. Xiao, J. C. Zhou, C. H. Yan, *ACS Nano* **2013**, *7*, 7200; b) D. Yang, P. a. Ma, Z. Hou, Z. Cheng, C. Li, J. Lin, *Chem. Soc. Rev.* **2015**, *44*, 1416.
[13] a) L.-D. Sun, Y.-F. Wang, C.-H. Yan, *Acc. Chem. Res.* **2014**, *47*, 1001; b) Q. Liu, W. Feng, F. Li, *Coord. Chem. Rev.* **2014**, *273/274*, 100; c) Y.-F. Wang, G.-Y. Liu, L.-D. Sun, J.-W. Xiao, J.-C. Zhou, C.-H. Yan, *ACS Nano* **2013**, *7*, 7200.
[14] a) P. Agostinis, K. Berg, K. A. Cengel, T. H. Foster, A. W. Girotti, S. O. Gollnick, S. M. Hahn, M. R. Hamblin, A. Juzeniene, D. Kessel, M. Korbelik, J. Moan, P. Mroz, D. Nowis, J. Piette, B. C. Wilson, J. Golab, *CA Cancer J. Clin.* **2011**, *61*, 250; b) T. J. Dougherty, C. J. Gomer, B. W. Henderson, G. Jori, D. Kessel, M. Korbelik, J. Moan, Q. Peng, *J. Natl. Cancer Inst.* **1998**, *90*, 889; c) P. R. Ogilby, *Chem. Soc. Rev.* **2010**, *39*, 3181.
[15] G. Tian, W. Ren, L. Yan, S. Jian, Z. Gu, L. Zhou, S. Jin, W. Yin, S. Li, Y. Zhao, *Small* **2013**, *9*, 1929.
[16] S. Zonghai, H. Dehong, X. Miaomiao, H. Meng, G. Ping, C. Lintao, *Nano-Micro Lett.* **2013**, *5*, 145.
[17] a) Z. Sheng, D. Hu, M. Zheng, P. Zhao, H. Liu, D. Gao, P. Gong, G. Gao, P. Zhang, Y. Ma, L. Cai, *ACS Nano* **2014**, *8*, 12310; b) R. Chen, X. Wang, X. Yao, X. Zheng, J. Wang, X. Jiang, *Biomaterials* **2013**, *34*, 8314.
[18] C. Guo, S. Yin, M. Yan, M. Kobayashi, M. Kakihana, T. Sato, *Inorg. Chem.* **2012**, *51*, 4763.
[19] Y. Liu, Y. Li, X.-M. Li, T. He, *Langmuir* **2013**, *29*, 15275.
[20] a) C.-H. Lee, S.-H. Cheng, Y.-J. Wang, Y.-C. Chen, N.-T. Chen, J. Souris, C.-T. Chen, C.-Y. Mou, C.-S. Yang, L.-W. Lo, *Adv. Funct. Mater.* **2009**, *19*, 215; b) J. S. Souris, C.-H. Lee, S.-H. Cheng, C.-T. Chen, C.-S. Yang, J.-a. A. Ho, C.-Y. Mou, L.-W. Lo, *Biomaterials* **2010**, *31*, 5564.
[21] I. B. C. Matheson, J. Lee, B. S. Yamanashi, M. L. Wolbarsht, *J. Am. Chem. Soc.* **1974**, *96*, 3343.
[22] a) Y. Liu, Y. Liu, W. Bu, C. Cheng, C. Zuo, Q. Xiao, Y. Sun, D. Ni, C. Zhang, J. Liu, J. Shi, *Angew. Chem. Int. Ed.* **2015**, *54*, 8105; b) S. S. Lucky, N. Muhammad Idris, Z. Li, K. Huang, K. C. Soo, Y. Zhang, *ACS Nano* **2015**, *9*, 191.
[23] M. P. Melancon, M. Zhou, C. Li, *Acc. Chem. Res.* **2011**, *44*, 947.
[24] L. Cheng, H. Gong, W. Zhu, J. Liu, X. Wang, G. Liu, Z. Liu, *Biomaterials* **2014**, *35*, 9844.
[25] a) P. Cherukuri, E. S. Glazer, S. A. Curley, *Adv. Drug Delivery Rev.* **2010**, *62*, 339; b) D. Jaque, L. Martinez Maestro, B. del Rosal, P. Haro-Gonzalez, A. Benayas, J. L. Plaza, E. Martin Rodriguez, J. Garcia Sole, *Nanoscale* **2014**, *6*, 9494.
[26] a) H. Gong, Z. Dong, Y. Liu, S. Yin, L. Cheng, W. Xi, J. Xiang, K. Liu, Y. Li, Z. Liu, *Adv. Funct. Mater.* **2014**, *24*, 6492; b) Y. Wang, H. Wang, D. Liu, S. Song, X. Wang, H. Zhang, *Biomaterials* **2013**, *34*, 7715.
[27] C. Guo, S. Yin, M. Yan, M. Kobayashi, M. Kakihana, T. Sato, *Inorg. Chem.* **2012**, *51*, 4763.
[28] Y. Liu, Y. Li, X. Li, T. He, *Langmuir* **2013**, *29*, 15275.